Distinct mural cells and fibroblasts drive fibrochondrogenesis in retrodiscal tissue following temporomandibular joint disc displacement

Wenlin Yuan[1], Yilin Chen[1], Ruojin Yan[2, 3, 4, 5, 6], Wei Liu[1], Chenyu Wang[1], Ying Wang[1], Qiaoli Dai[1], Wen Li[1], Mengqi Zhu[1], Xiao Chen[7, 3, 5], Jiejun Shi[1]

1 Stomatology Hospital, School of Stomatology, Zhejiang University School of Medicine, Zhejiang Provincial Clinical Research Center for Oral Diseases, Key Laboratory of Oral Biomedical Research of Zhejiang Province, Cancer Center of Zhejiang University, Engineering Research Center of Oral Biomaterials and Devices of Zhejiang Province, Hangzhou, China. 2 Dr. Li Dak Sum & Yip Yio Chin Center for Stem Cells and Regenerative Medicine and Department of Orthopedic Surgery of Sir Run Shaw Hospital, Zhejiang University School of Medicine, Hangzhou, China. 3 Liangzhu Laboratory, Zhejiang University, 1369 West Wenyi Road, Hangzhou, China. 4 Key Laboratory of Tissue Engineering and Regenerative Medicine of Zhejiang Province, Zhejiang University School of Medicine, Hangzhou, China. 5 Department of Sports Medicine, Zhejiang University School of Medicine, Hangzhou, China. 6 China Orthopedic Regenerative Medicine Group (CORMed), Hangzhou, China. 7 Department of Sports Medicine & Orthopedic Surgery, The Second Affiliated Hospital, and Dr. Li Dak Sum & Yip Yio Chin Center for Stem Cells and Regenerative Medicine, Zhejiang University School of Medicine, Hangzhou, China.

Address correspondence to: Jiejun Shi, Affiliated Hospital of Stomatology, School of Medicine, Zhejiang University, No. 166 Qiutao North Road, Hangzhou, China. Phone: 86.571.87216723; Email: sjiejun@zju.edu.cn. or Xiao Chen, 1 Department of Sports Medicine & Orthopedic Surgery,

The Second Affiliated Hospital, and Dr. Li Dak Sum & Yip Yio Chin Center for Stem Cells and Regenerative Medicine, 2 Liangzhu Laboratory, Zhejiang University School of Medicine, No. 866 Yuhangtang Road, Hangzhou, China. Phone: 86.571.88208442; Email: chenxiao-610@zju.edu.cn.

Authorship note: WY and YC contributed equally to this work. Correspondence should be addressed to JS and XC.

Conflict of interest: The authors have declared that no conflict of interest exists.

Abstract

Adaptive remodeling of retrodiscal tissue following anterior disc displacement (ADD) of the temporomandibular joint (TMJ) has been recognized for decades, yet the underlying cellular dynamics and molecular mechanisms remain unclear. Using a porcine ADD model, this study investigated the cellular and molecular basis driving retrodiscal tissue adaptation. Histological staining revealed adaptive remodeling of retrodiscal tissue after ADD induction, with dense connective tissue and cartilaginous masses replacing loose connective tissue. Furthermore, single-cell RNA sequencing (scRNA-seq) captured pronounced fibroblast expansion during tissue remodeling, notably the FB2 subcluster with high developmental potential, and the emergence of a mural cell subcluster MC4 associated with extracellular matrix (ECM) remodeling. CellChat analysis highlighted MC4-FB2 crosstalk via FGF2 and BMP5 signaling. The combination of pathway-aware multi-layered hierarchical network (P-NET) and Seurat with drug database screening identified five promising compounds. Among them, Zaprinast demonstrated the most robust effects by enhancing the remodeling capability of fibroblasts in vitro, and also alleviated TMJ deformation in vivo. Collectively, fibroblast activation is pivotal for early retrodiscal tissue adaptation following ADD, which is driven by MC4-derived FGF2/BMP5 signaling. Zaprinast treatment potentiates this remodeling process. These findings provide new insights into cellular basis of TMJ adaptation and identify potential therapeutic targets for ADD management.

Introduction

Anterior disc displacement (ADD) of the temporomandibular joint is the most common subtype of temporomandibular disorders (TMD), characterized by the forward shifting of the disc from its normal position (1, 2). Studies have reported the association between ADD and the development of osteoarthrosis (OA) (3). Magnetic resonance imaging (MRI) findings in ADD patients revealed joint effusion and degenerative changes including bone erosion, grinding and osteophyte formation (4). However, clinical observations indicate that some ADD patients remain asymptomatic or only exhibit transient symptoms, with many remaining long-term temporomandibular joint (TMJ) stability (5). Variations in clinical outcomes suggest that individuals have differential adaptive capacities in response to traumatic intra-articular movements, which are closely related to the response of the retrodiscal tissue.

The retrodiscal tissue is attached posterior to the articular disc. It is mainly composed of loose connective tissue, richly vascularized, and covered by synovial tissue (6). Compared to the disc, its load-bearing capacity is much weaker (7). Following ADD, part of the retrodiscal tissue is positioned above the condyle and subjected to abnormal stress. Under this condition, the retrodiscal tissue may undergo two distinct types of changes. One is destructive, characterized by degenerative changes involving the breakdown of collagen or elastic fibers, often accompanied by inflammation. The retrodiscal tissue eventually becomes thinner or even perforated, resulting in persistent pain and dysfunction (8). The other is adaptive, including conversion of the loose connective tissue to dense connective tissue or even forming a fibrocartilage-like

structure capable of bearing abnormal loads (9, 10). When tissue remodeling is sufficient, the retrodiscal tissue may acquire structural similarities to the disc, thereby expanding the range of area that can withstood stress during condyle motion. Thus, some researchers have proposed that enhancing adaptive remodeling of retrodiscal tissue by eliminating unfavorable factors, therapeutic effect can be achieved even if the disc displacement is not resolved.

Adaptive remodeling of the retrodiscal tissue has been recognized for decades. In a rat ADD model, the retrodiscal tissue progressively transformed into dense fibrous tissue with marked reduction in adipose content 8 weeks after ADD induction (9). Gu et al. (10) observed chondrocyte differentiation in the retrodiscal tissue by detecting type II collagen mRNA expression in a rabbit ADD model at 1 week, while typical cartilage tissue was apparent by 2 weeks. Longitudinal study of patients with ADD without reduction (ADDwoR) over a period of 4-8 years revealed pseudo-disc like changes in the retrodiscal tissue in 45% of patients (11). Histological examinations have also documented the presence of dense fibrous tissue containing scattered chondrocytes and increased glycosaminoglycan (GAG) content in some ADD patients (12, 13). Nevertheless, the cellular and molecular mechanisms driving this remodeling process remain poorly understood.

Compared with rodents, porcine TMJ more closely resembles human TMJ in bilateral occlusion, translational movement, disc structure, and biomechanical function (14, 15). These characteristics make pigs particularly suitable for TMD research. Moreover, suture-induced ADD animal modeling fails to replicate human disease

progression, as the traction forces generated are inconsistent and difficult to control. In contrast, elastic traction allows quantifiable force adjustment and provides sustained force to produce stable and reproducible results (16). In this study, we established a porcine unilateral ADD (UADD) model using surgical intervention with a titanium spring, and performed single-cell RNA sequencing (scRNA-seq) analysis of TMJ disc and retrodiscal tissue 5 weeks post-ADD induction. We aimed to resolve the cellular heterogeneity in disc and retrodiscal tissue, and capture critical transcriptional changes and cellular drivers promoting adaptive remodeling of retrodiscal tissue.

Results

ScRNA-seq resolves cell heterogeneity in porcine discs and retrodiscal tissues

To understand the composition and molecular profiles of cells in different regions and pathological states, we profiled cells from the sham operation and UADD models using scRNA-seq. TMJ samples with sham operation were collected as SHAM group. In the UADD model, TMJ samples from the ADD induction side (ADD group) and the contralateral side (CADD group) were collected, respectively. The overall workflow of the sample dissociation and single-cell RNA sequencing is shown in Figure 1A. An unsupervised clustering algorithm partitioned the cells into 7 separated clusters (Supplemental Figure 1C), which were classified into five principal cell types: the endothelial cells (ECs), the fibroblasts (FBs), the mural cells (MCs), the immune cells (ICs) and the cells in cell cycle (Cycle) (Figure 1, B and C). Markers used to annotate each cell cluster are presented in Figure 1E (17, 18). The top 5 differentially expressed genes in each cluster were shown in Figure 1F.

The distribution and proportion of cell clusters according to their origin were also evaluated. Stacked bar plots showed the proportion of the main cell types in disc and retrodiscal tissue (Figure 1D). Among major cell types, FBs and ECs composited the vast majority of cells. Unlike rodents, whose TMJ discs are mostly composed of fibroblasts, porcine discs contain a substantial vascular component. This is consistent with recent studies that the TMJ disc of higher-order species is in fact vascularized and exhibits higher angiogenic gene expression compared with knee meniscus (14, 17).

Adaptive remodeling occurs in retrodiscal tissues after ADD induction

To define histological changes after ADD induction, we applied hematoxylin-eosin (H&E) staining and alcian blue staining. The disc from SHAM group was characterized by anterior-posterior fiber alignment in the intermediate zone, with spindle-shaped fibroblasts and round-shaped chondrocyte-like cells distributed in the dense connective tissue. However, the retrodiscal tissue from the SHAM group exhibited relatively loose and irregular connective tissue, with interspersed adipose tissue (Figure 1G). Furthermore, alcian blue staining was observed in discs, with the intermediate zone showing the strongest intensity. In contrast, the retrodiscal tissue appeared almost no alcian blue staining (Figure 1H). Different GAG contents in disc and retrodiscal tissue closely correlate with the mechanical demands they are subjected to (19). After ADD induction, small fissures were found among collagen fibers, with slightly reduced GAG content in the disc from ADD and CADD groups. These indicated weaken mechanical property of TMJ disc in both ADD and contralateral sides. In retrodiscal tissue from the ADD and CADD groups, part of the loose connective tissue and adipose tissue were replaced by dense connective tissue and accompanied by fibroblast proliferation. Concurrently, we found cartilaginous masses emerged in the retrodiscal tissue by alcian blue staining (Figure 1, G and H). Importantly, the condyle underneath didn't exhibit overt degenerative changes after ADD induction (Supplemental Figure 2). Overall, these results revealed adaptive remodeling of the retrodiscal tissue on both ADD and CADD sides, with fibrosis and chondrogenesis as the main manifestations.

We further investigated transcriptional changes in the disc and retrodiscal tissue

following ADD induction and captured changes in cell proportion of main cell types. Compared with the SHAM group, discs from ADD and CADD groups showed minor changes in main cell proportions, whereas retrodiscal tissues revealed remarkable changes, typically characterized by an increase in fibroblasts (Figure 1D). These findings suggest that the retrodiscal tissue is highly adaptive and sensitive to mechanical stress. Fibroblast proliferation in the retrodiscal tissue likely facilitates load bearing during joint movement.

Identification of responsive FB subtypes participating in adaptive remodeling of the retrodiscal tissue

As fibroblasts are known to play central roles in extracellular matrix (ECM) homeostasis and remodeling (20), we further investigated their composition in detail. Unsupervised clustering divided fibroblasts into six subclusters (FB1-FB6) (Figure 2, A and B). The differentially expressed genes (DEGs) (Figure 2D) and Gene Ontology (GO) enrichment analysis (Figure 2E) of each FB subclusters were utilized to define their identities. FB1 represented the predominant fibroblast population in both disc and retrodiscal tissue, but its proportion in the disc decreased markedly after ADD. FB1 preferentially expressed *PTN*, supporting fibroblast proliferation and function (21). FB2 was distinguished by signature genes related to cholesterol metabolism (*APOE*) and ECM integrity (*EFEMP1*) (22, 23). GO analysis further revealed that FB2 was enriched in functions related to cell differentiation, wound healing and response to fibroblast growth factor. In the SHAM group, FB2 proportions were similar in both disc

and retrodiscal tissue. In contrast, FB2 showed a substantial increase in the retrodiscal tissue of ADD and CADD groups, indicating it is highly responsive and may play an active role in tissue remodeling. FB3 expressed *COMP* and *FMOD*, genes involved in collagen biosynthesis, ECM assembly and cartilage composition (24, 25). FB4 displayed high expression of *PRSS35* and *ENSSSCG00000029449* (proteoglycan 4, *PRG4*), suggesting a role in cellular homeostasis under stress environment and lubrication (26, 27). Genes such as *CD74* and *PECAM1* were expressed by FB5, indicating its function in regulating cell migration and angiogenesis. FB6 accounted for a minor fraction of fibroblasts and was associated with epithelial junctions and muscle development (Figure 2, D and E).

To better understand the function of porcine TMJ fibroblasts, we compared their transcriptomic profiles with murine TMJ disc fibroblasts at different postnatal stages (17). Correlation analysis demonstrated that porcine FB1 and FB2 are most similar to murine FB1 (fibroblast associated with fibrillogenesis and fibrillary homeostasis), whereas porcine FB3 resembles murine FB6 (chondrogenesis related fibroblast). However, correlation coefficients were generally low (approximately 0.2), highlighting substantial interspecies heterogeneity (Supplemental Figure 3).

TMJ tissues undergo continuous ECM remodeling processes to maintain microenvironment homeostasis. Given the central role of fibroblasts in ECM organization, we investigated ECM expression patterns across FB subtypes. The dot plot shows dynamic ECM gene expressions among FB clusters (Figure 2F). The main constitutive collagen genes *COL1A1* and *COL1A2* were highly expressed in FB3 and

moderately expressed in FB1. A small proportion of FB3 also expressed fibrocartilage-associated genes *ACAN*, *CHAD* and *COMP*, suggesting FB3 as a key subcluster contributing to ECM composition. In contrast, the remaining FB subclusters primarily modulated ECM formation and assembly. FB2 expressed non-fibrillar collagen gene *COL4A2*, which functions in connective tissue anchoring and basal lamina formation (28). FB4 regulated collagen fibrillogenesis and ECM assembly by *LUM* and *FN1* expressions (29). Meanwhile, FB5 and FB6 were enriched for secreted factors including *EGFL7*, *S100A4* and *SFRP1*, *BMP7*, supporting roles in angiogenesis and myotendinous junction development (30, 31).

We further used pseudotime trajectory analysis to predict differentiation states of FB clusters. The FB2 has optimal development potential (Supplemental Figure 4), and serves as progenitor cells which differentiate towards two directions, ECM producing FBs (FB1, FB3) and modulatory FBs (FB4-6) (Figure 2, G-I). Studies have shown that EGF-like fibulin extracellular matrix protein 1 (EFEMP1) plays a role in maintaining the immature status of cells in the cartilage superficial zone, while apolipoprotein E (APOE) is identified as a marker of chondrocytes in the resting zone of growth plate (23, 32). These findings enlighten us again that FB2 is highly responsive during adaptive remodeling. Additionally, results from immunofluorescence staining are consistent with our bioinformatic analyses. APOE positive cells significantly increased and presented higher proliferative properties within the retrodiscal tissue from ADD and CADD groups compared with SHAM group (Figure 2, J and K, Supplemental Figure 5).

Additionally, we analyzed gene expression changes between the experimental (ADD+CADD) RT group and SHAM RT group. Compared with the SHAM group, fibroblasts from experimental group showed alteration in genes related to ECM organization and turnover (*COL3A1*, *WISP2*, *COMP*, *FMOD* and *CST3*) (33, 34). Concurrently, genes associated with fibroblast proliferation and apoptosis (*BTG2* and *IFI6*) were also differentially expressed (Supplemental Figure 6A) (35, 36).

Specifically, fibroblasts from CADD RT group were characterized by ECM remodeling related genes (*COL3A1*, *COL11A1* and *FMOD*), indicating enhanced ECM synthesis and reorganization. Fibroblasts from ADD RT group exhibited a stress-activated profile (*CCL2*, *CCL19* and *SOD2*) (37), suggesting injury-induced inflammation and compensatory repair processes. In contrast, fibroblasts from SHAM RT group predominantly expressed genes involved in maintaining ECM homeostasis and progenitor cell recruitment (*CXCL12*, *CST3* and *COMP*) (Supplemental Figure 6B) (34, 38).

Collectively, these findings support a transcriptional shift toward an activated, ECM-remodeling related fibroblast phenotype following ADD.

A specific ECM-related mural cell subcluster emerges in retrodiscal tissue after ADD induction

Mural cells are essential components of blood vessels, which attach to the surface of vascular endothelial cells and maintain vasculature stability (39). Some studies have also suggested their pivotal roles in fibrosis (40). Among four MC subclusters, MC1,

MC3 and MC4 displayed high expression of *ACTA2*, *CNN1* and *MYH11*, indicating a smooth muscle cell (SMC) identity, while MC2 was identified as pericytes by its high expression of *HIGD1B*, *RGS5* and *NUDUFA4L2* (Supplemental Figure 7, A and B). We further defined MC1 as typical SMC due to its high expression of *MYH11* and *ACTA2*. MC3 was named as immune-related SMC with its expression of *CD74*, while MC4 was considered as ECM-related SMC owing to its specific expression of *DCN*, *COL1A1* and *COL1A2* and its biological association with ECM organization (Figure 3, D and E). Interestingly, MC4 was nearly absent in the retrodiscal tissue from SHAM group but increased in ADD and CADD groups (Figure 3C). Pseudotime trajectory analysis revealed that MC4 differentiated from pericyte (MC2), and pericyte could also differentiate into typical SMC (MC1) and immune-related SMC (MC3) (Supplemental Figure 7, C and D). The absence of MC4 in retrodiscal tissue from SHAM group, and presence of the MC4 in retrodiscal tissue from ADD and CADD groups were further confirmed using immunofluorescence staining (Figure 3F).

We further evaluated subtle transcriptional changes in other cell clusters after the onset of ADD. Four EC subclusters were identified as vein ECs, capillary ECs, artery ECs and lymphatic ECs (Supplemental Figure 8A). The capillary ECs with high angiogenesis potential decreased in retrodiscal tissue of the ADD and CADD groups, suggesting inhibited angiogenesis during tissue remodeling (Supplemental Figure 8B) (41). With regard to immune cells, they were more abundant and diverse in the retrodiscal tissue than the disc, indicating that the retrodiscal tissue may be more immunologically active. The percentages of macrophages and neutrophils increased in

retrodiscal tissue after ADD (Supplemental Figure 8, C and D).

Putative signaling network for the intercellular crosstalk regulating adaptive remodeling of the retrodiscal tissue

To probe differences in cell-cell communication between SHAM RT and ADD RT groups, as well as between SHAM RT and CADD RT groups, we employed comparative CellChat. A total of 13 cell clusters, including ECs, ICs, Cycle and subclusters of FBs and MCs were combined for analysis. Network centrality analysis was performed by computing the outgoing and incoming interaction strengths of each cell subpopulation to assess their likelihood as signaling sources and targets, respectively. In SHAM RT group, interactions between fibroblast subclusters (mainly FB1 and FB3) and other cells were most intense. In contrast, the newly emerged MC4 subcluster showed drastically increased interactions with other cells after ADD (Supplemental Figure 9B). We further compared the information flow, defined by the sum of communication probability among all pairs of cell groups in the inferred network (Supplemental Figure 9C). Pathways including MK, PERIOSTIN, FGF, BMP, TWEAK, SPP1, IL6 and MIF were exclusively active in both ADD RT and CADD RT groups, indicating enhanced cell proliferation, migration and differentiation (42-47). Other pathways such as GAS, PDGF and VISFATIN revealed decreased information flow after ADD induction, which are known to be associated with fibroblast inhibition, vascular development and inflammatory responses (48-50).

Next, we investigated the candidate pathways underlying the changes in cellular

compositions and tissue features after ADD induction. The newly emerging MC4 cluster exhibited extensive potential for both self- and reciprocal interactions in ADD RT and CADD RT groups, such as TGF-β, FGF and BMP pathways (Figure 4, A-D). We speculated that MC4 may be an important regulator of tissue remodeling. Active fibroblast-MC4 interactions were also found, particularly enriched in the FGF and BMP signaling (Figure 4, E and F). In ADD RT group, FGF signaling exhibited intensive exchanges between fibroblasts and mural cells, whereas the BMP signaling were mainly sent by MC4 and received by FB subclusters. In CADD RT group, MC4 presented as the only sender of FGF signaling, and all FB subclusters were considered as receivers. Notably, interaction between FB2 and MC4 via FGF signaling was particularly intense. BMP signaling was sent by MC1 and MC4, while received mainly by MC4, FB2 and FB3 (Figure 4, E and F). Specifically, the receptor-ligand signaling communication probabilities from MC4 to FBs showed that FGF2-FGFR1 and BMP5-BMPRA1+BMPR2 are the major contributors in FGF signaling and BMP signaling, respectively (Supplemental Figure 10). Immunofluorescence staining demonstrated markedly increased expression of FGF2 and BMP5 in mural cells within the retrodiscal tissue of ADD and CADD groups (Supplemental Figure 11, Supplemental Figure 12), supporting the predicted signaling activity in vivo.

In vitro functional experiments showed that TGF-β treatment markedly induced transformation of mural cells into MC4, as indicated by enhanced expressions of fibroblast (FN1, COL1A1 and DCN) and smooth muscle cell (ACTA2) markers (Figure 4, G-J). Consistently, TGF-β induced transition of mural cells toward the MC4

phenotype resulted in elevated FGF2 and BMP5 levels (Figure 4J). In addition, conditioned medium from MC4 enhanced ECM deposition and chondrogenic marker expression in fibroblasts (Figure 4, K and L). Consistent with our in vitro findings, FGF2 and BMP5 treatment exhibited synergistic effects on enhancing ECM synthesis and chondrogenic differentiation of fibroblasts (Supplemental Figure 13).

To reveal the underlying mechanism, we evaluated changes of classical pathways activated by FGF2 and BMP5, including the ERK1/2 and SMAD1/5/9 cascades. We observed the activation of ERK1/2 pathway as early as 6 hours after stimulation, followed by the activation of SMAD1/5/9 cascade about 24 hours after stimulation (Figure 4M). These results indicate that MC4 induces sequential activation of distinct pathways to orchestrate the phenotypic transition of fibroblasts. The early activation of ERK1/2 signaling likely drives fibroblast proliferation and ECM deposition, initiating retrodiscal tissue remodeling. As remodeling progresses, the SMAD1/5/9 signaling become progressively enhanced, promoting ECM reorganization and inducing fibrocartilage formation.

Selection of candidate compounds enhancing remodeling capability of fibroblasts

To identify drugs that enhance fibroblast remodeling, we focused on predicted drug responses associated with feature genes from fibroblast subsets. We combined top-ranked genes from a pathway-aware multi-layered hierarchical network (P-NET) and Seurat with the medicine database (ConnectivityMap and DGIdb) to seek for candidate compounds. The screening workflow is shown in the schematic diagram (Supplemental

Figure 14).

Molecular profiles of fibroblasts by comparing SHAM RT and ADD RT, SHAM RT and CADD RT groups were fed into P-NET, which maps genes onto a hierarchical network of weighted nodes (51). We visualized the top 10 most important nodes using Sanky diagrams to reveal the interaction between different features, genes, pathways and biological processes and to study the paths of impact from the input to the outcome (Supplemental Figure 15, A and B). Highly ranked genes in both ADD and CADD groups included *CST3*, *FGL2* and *B2M*. *CST3* encodes Cystain C, a cysteine proteases inhibitor that promotes matrix deposition and is overexpressed in cardiac, lung or liver fibrosis (34, 52). Fibrinogen-like protein 2 (FGL2) regulates the polarization of macrophages (53), and is enriched in ADD patients without OA compared to those with OA (54). *B2M* encodes β2-microglobulin, a serum protein with antibacterial activity (55). After ADD induction, processes relating to metabolism of proteins, gene expression, metabolism of RNA and cell cycle support adaptive remodeling as a condition with large systemic effects on metabolism, immune and cellular homeostasis. In fibroblasts from CADD RT, *COL1A1*, *COL1A2* and *COL3A1* ranked in the top 10 and were associated with collagen formation and ECM organization, consistent with histological observations that CADD RT exhibited superior tissue remodeling compared to ADD RT.

Five candidate compounds were identified after scoring with the gene expression feature data from the medicine database (Supplemental Table 2). According to their mechanism of action (MOA), potential targets and score ranking, 3 molecules

(Batimastat, Sunitinib and Zaprinast) were selected for in vitro testing. Batimastat is a broad-spectrum peptide inhibitor of matrix metalloproteinases (MMPs), which exerts therapeutic effects in heart failure and pulmonary fibrosis by MMPs inhibition (56, 57). Sunitinib is a tyrosine kinase inhibitor targeting vascular endothelial growth factor (VEGF) and platelet-derived growth factor receptor (PDGFR) receptors. It shows notably efficiency in advanced renal cell carcinoma and intolerant gastrointestinal stromal tumor treatment (58), but may induce side effects such as cardiac fibrosis (59). Zaprinast is a phosphodiesterase 5 (PDE5) inhibitor and G protein-coupled receptor 35 (GPR35) agonist, targeting inflammation and pain reduction (60, 61). However, reports on its activity in the regulation of ECM remodeling are currently lacking.

Cytotoxicity of the selected compounds was assessed using CCK-8 assays. Batimastat (1-100 nM) and Zaprinast (0.1-100 μM) possessed good biocompatibility to porcine fibroblasts, whereas sunitinib exhibited significant cytotoxicity even at 1 nM (Supplemental Figure 15, C-E). We further determined the optimal drug concentration by evaluating the of target gene expressions (Supplemental Figure 15, F-H). 10 nM Batimastat, 1 nM sunitinib and 1 μM Zaprinast were used in the following experiments.

We next investigated the effect of these compounds on ECM synthesis and chondrogenesis in fibroblasts. QRT-PCR and western blot (WB) analyses revealed that Sunitinib and Zaprinast markedly increased ECM gene expression, whereas Batimastat had minimal effect (Figure 5, A and B). Under chondrogenic induction, fibroblasts treated with Zaprinast showed highest expression of chondrogenic differentiation markers compared with Batimastat and Sunitinib (Figure 5, C and D). As shown by

immunofluorescence staining, Zaprinast significantly increased the expression of COL1A1 and APOE in fibroblasts (Figure 5, E-H). Notably, elevated APOE expression indicates enhanced remodeling capacity in fibroblasts, a characteristic feature of the FB2 phenotype. Alcian Blue staining and immunofluorescence staining (SOX9, ACAN, COL2A1) of pellet culture under chondrogenic differentiation further confirmed its effects on chondrogenesis (Figure 5, I-M). Mechanistically, Zaprinast promoted fibrocartilage differentiation of fibroblasts through activating the ERK1/2 and SMAD1/5/9 pathways, the canonical downstream pathways of FGF2 and BMP5 (Figure 5, N and O). In summary, Zaprinast appeared to have optimal effects in enhancing ECM synthesis and chondrogenic differentiation of fibroblasts.

Zaprinast alleviates disc and retrodiscal tissue deformation and mitigates condyle damage in vivo

We investigated whether Zaprinast could promote adaptive remodeling of the retrodiscal tissue and maintain condyle integrity following ADD in vivo. Zaprinast was administered intraperitoneally before and after ADD induction (Figure 6A). In the SHAM+Vehicle group, the disc remained thin and well-oriented. Five weeks after ADD induction, the ADD+Vehicle group exhibited alterations including thickening and anterior displacement of the disc, disorganized collagen architecture in the posterior band and retrodiscal tissue, and inflammatory cell infiltration. These pathological changes were partially alleviated by Zaprinast treatment, which exhibited improved orientation and organization of collagen fibers (Figure 6, C and D). During the observation period, no perforations or tears were observed in the disc or retrodiscal

tissue in any group. We did not observe fibrocartilage formation in the rat model, likely reflecting species-specific differences in masticatory patterns and TMJ anatomy.

We further assessed changes in condylar cartilage and subchondral bone. H&E staining revealed hyperplasia of the superficial fibrous layer and irregularities of the cartilage in the ADD+Vehicle group compared with the SHAM+Vehicle group. Consistently, the safranin-O and fast green (SO/FG) staining demonstrated substantial loss of cartilage matrix in the ADD+Vehicle group. Micro-computed tomography (Micro-CT) analysis revealed condylar flattening (Figure 6B), reduced bone volume fraction (BV/TV), decreased trabecular number (Tb.N), and increased trabecular spacing (Tb.Sp) (Figure 6, E-H). Zaprinast treatment mitigated degenerative changes in cartilage morphology (Figure 6I), increased cartilage matrix content (Figure 6J) and partially restoring subchondral bone morphology (Figure 6, E-H).

In summary, these findings indicate that Zaprinast partially restores the ordered structure of the disc and retrodiscal tissue, and concurrently attenuates cartilage matrix loss and subchondral bone resorption after ADD induction.

Discussion

Clinical observations indicate that most TMD cases follow a mild and fluctuating course. In natural course of ADDwoR patients, their clinical symptoms tend to alleviate, with improvements in mandibular movement and masticatory efficiency (62), suggesting that TMJ has a remarkable adaptive capacity. Following ADD, mechanical load shifts from the articular disc to the mechanically inferior retrodiscal tissue. Finite element (FE) analysis has confirmed that perforations in retrodiscal region show higher maximum equivalent stress than perforations in other areas, explaining why perforation predominantly occurs at the retrodiscal tissue (63). Moreover, retrodiscal attachment dissection hastens ADD progression (64), whereas adaptive remodeling correlates with condylar cartilage recovery (9). These findings underscore the importance of retrodiscal tissue integrity and remodeling for TMJ stability.

Our UADD porcine model revealed bilateral retrodiscal tissue adaptation, highlighting the need to monitor both affected and contralateral joints in clinic. ScRNA-seq analysis revealed cellular heterogeneity between TMJ disc and retrodiscal tissue, identifying key cell subpopulations driving remodeling. Cell-cell communication analysis implicated FGF and BMP signaling as critical regulators. Using biologically-informed deep learning, we identified Zaprinast as a potential therapeutic compound that promotes adaptive remodeling of retrodiscal tissue and prevented TMJ damage at the early stage of ADD.

Despite remodeling of retrodiscal tissue after ADD has been recognized for decades, detailed cellular mechanisms remained unclear due to technical limitations. ScRNA-

seq analysis provided a systematic view of cell diversity between TMJ disc and retrodiscal tissue, revealing dynamic changes after ADD. In pigs that underwent sham operation, the retrodiscal tissue exhibited a cell composition broadly similar to that of the disc but with distinct relative proportions, supporting its inherent potential for disc-like transformation. Notably, a developmentally potent FB2 subpopulation increased after ADD. We identified several features of FB2 that may drive remodeling. FB2 predominantly express resident progenitor cell marker genes *APOE* and *EFEMP1* (23, 32). Pseudotime trajectory analysis revealed that FB2 could differentiate into ECM producing FB (FB1, FB3) and modulatory FB (FB4-6). FB3, in particular, displayed fibrocartilaginous characteristics by predominant expression of *COL1A1*, *COL1A2*, *ACAN* and *COMP*. Histology evaluation confirmed GAG accumulation in retrodiscal tissue after ADD, supporting mechanical-induced adaptation (6). These findings suggest that FB2 is important for fibroblast expansion and ECM deposition during adaptive remodeling.

Apart from the reparative role of FBs, the supporting role of minor cell populations is also noteworthy. ScRNA-seq analysis and lineage tracing studies verified that pericytes transiently express fibroblast markers and contribute to vascular maturation after myocardial infarction (40). Similarly, a new mural cell subtype (MC4) emerged after ADD, displaying ECM-related signatures and broad interactions with other cells. TGF-β predominantly participated in MC4 self-interaction, aligning with its profibrotic role in promoting fibroblast proliferation, ECM synthesis, and myofibroblast differentiation (65). In vitro, TGF-β induced MC4 phenotype in mural cells, and co-

culture with fibroblasts further indicate MC4's paracrine regulation in fibroblast activation.

Abnormal loading can induce fibrocartilaginous metaplasia and ligament ossification via Hedgehog and BMP signaling (66, 67). We identified increased pathways in ADD RT and CADD RT groups including PERIOSTIN, FGF, BMP, TWEAK, SPP1 and IL6, which are closely related to fibrosis (43-46). Notably, FGF and BMP signaling were engaged in MC4 to FB interactions, promoting fibroblast expansion and chondrogenic differentiation. These findings are consistent with observations in fibrotic OA synovial tissues, where FGF and BMP drive ECM remodeling, contrasting with inflammatory phenotypes dominated by predominant inflammatory cytokine expressions and pain (68). MC4-derived signals modulate fibroblast behavior through coordinated activation of ERK1/2 and SMAD1/5/9 pathways. FGF2 is a well-established activator of ERK1/2, and ERK activation can indirectly potentiate BMP-SMAD1/5/9 signaling (69) and directly phosphorylate SMAD4 (70). BMP5 activates both canonical SMAD and non-canonical MEK-ERK pathways in developmental and neural crest contexts (71). These observations suggest that MC4-derived FGF2 and BMP5 may act synergistically to amplify ERK1/2-SMAD1/5/9 signaling, thereby promoting fibroblast remodeling.

By combining a causal-inspired (P-NET) approach with a correlation-based (Seurat) approach, we identified high-confidence candidate targets that support tissue adaptation during ADD, which are both statistically correlated and biologically interpretable. Five potential compounds were identified, with Zaprinast showing superior efficacy in enhancing fibroblast remodeling. Furthermore, Zaprinast partly restored TMJ

deformation in rat ADD model, providing in vivo support for the therapeutic potential of Zaprinast. Previous studies have reported the osteogenic potential of Zaprinast by promoting angiogenesis and BMP synthesis (72). Similarly, another PDE inhibitor Sildenafil potentiates BMP signaling in pulmonary arterial smooth muscle cells by enhancing BMP4-induced phosphorylation of SMAD1/5 and inhibitor of DNA binding protein 1 expression (73). Mechanistically, our study revealed that Zaprinast promoted fibrocartilage differentiation of fibroblasts via ERK1/2 and SMAD1/5/9 pathways, which are canonical downstream of FGF2 and BMP5.

Given the limited availability of early-stage human ADD tissues, we employed a porcine model for its anatomical and physiological similarity to humans. Nevertheless, cross-species validation is essential, including validation of key cell subsets and pathways in human TMJ tissues and functional assessment in human-derived models. Pilot observational studies in humans could further determine whether the identified molecular signatures correlate with better clinical parameters. Long-term follow-ups in patients with non-reducing ADD and studies in animal ADD models indicate that retrodiscal tissue remodeling can serve as a beneficial process, leading to improved joint function (9-11). Nevertheless, dysregulated fibrosis may become maladaptive, contributing to joint stiffness and pain. Our findings suggest that MC4-mediated remodeling may initially support mechanical compensation, but future longitudinal studies are needed to determine whether it remains beneficial or transitions to pathological fibrosis.

Additionally, technical limitations include potential cell type bias during tissue

dissociation, which may underrepresent vulnerable populations such as adipocytes. Reduced adipose content in retrodiscal tissue may result from inhibited adipogenesis (74), lineage reprogramming of adipocytes into myofibroblasts (75) or stress-driven adipocyte apoptosis (76). Future studies using single-nucleus RNA-seq combined with functional validation are needed to clarify the contributions of adipocytes. The potential role of neuronal paracrine signaling in retrodiscal tissue remodeling also warrants future investigation.

In conclusion, our findings demonstrated that fibroblast activation is pivotal for early retrodiscal tissue adaptation following ADD, and is driven by the emerged ECM-remodeling MC subcluster. We implicate FGF and BMP signaling as key regulators of enhanced fibrosis and chondrogenic differentiation of fibroblasts by sequential activation of ERK1/2 and SMAD1/5/9 cascades. While current treatments for ADD lack targeted approaches for TMJ adaptation, our data suggest Zaprinast may be used as a promising drug for conservative treatment of ADD.

Methods

Sex as a biological variable

Our study examined female animals considering that TMD onset is more common in young women, potentially due to differences in hormonal factors, pain sensitivity and health-seeking behavior (77). Therefore, we utilized 5-month-old female Bama miniature pigs and 10-week-old female Sprague-Dawley rats that were considered sexually mature. Although we selected female pigs and rats in this study, we anticipate the fundamental mechanisms are applicable to both sexes.

Animals and groups

Four female Bama miniature pigs aged 5 months old and eighteen female Sprague-Dawley rats aged 10 weeks old were purchased from Zhejiang Chinese Medical University Laboratory Animal Research Center. Two pigs were randomly assigned to undergo sham operation on the left TMJ (SHAM group), while the right TMJ remained untreated. The other two pigs underwent ADD surgery on the left TMJ (ADD group), while the contralateral right TMJ was left untreated (CADD group). Rats were randomly divided into three groups: SHAM+Vehicle group (n=6), ADD+Vehicle group (n=6) and ADD+Zaprinast group (n=6). Zaprinast (MCE, USA) was dissolved in solvent (10% DMSO+40% PEG300+5% Tween-80+45% saline) and intraperitoneal injected 1 day before surgery and 1, 3, 5, 7, 10, 14, 21, 28 days after surgery (dosage: 10mg/kg (78)). An equivalent volume of solvent was administrated in vehicle groups.

Generation of unilateral anterior disc displacement (UADD) model

The surgical methods to generate UADD porcine model were modified according to previous study of rabbit models (16). Following intravenous anesthesia, the left preauricular region was shaved and disinfected. A 4 cm curved incision was made in line with the lateral canthus of the eye. After incising through subcutaneous tissue and periosteum, we reflected these layers to expose the zygomatic arch and TMJ capsule. The inferior joint space was carefully opened by dissecting the lateral capsule without damaging the TMJ disc or articular cartilage surface. The anterior and lateral attachments was partially released while preserving the posterior attachment.

Subsequently, an orthodontic mini-implant was screwed into zygomatic arch approximately 2 cm from its posterior margin. The stainless steel was used to connect the mini-implant and a nickel-titanium spring. To avoid osseointegration, a titanium-reinforced e-PTFE nonabsorbable membrane was placed between the zygomatic arch and nickel-titanium spring. After that, we penetrated the anterior attachment of articular disc with a 4-0 nylon suture and knotted it to posterior end of the nickel-titanium spring. By extending the spring from 4 mm to 14 mm, we applied 1 N of tension to displace the disc anteriorly, though immediate displacement wasn't observed. Finally, the wound was thoroughly irrigated with saline and closed in layers with a 3-0 monocryl sutures.

Similarly, rats were anesthetized with pentobarbital sodium (50mg/kg i.p.), and the left preauricular region was shaved and sterilized. After local anesthesia with lidocaine hydrochloride (2%), the zygomatic arch and lateral TMJ capsule was carefully opened to expose the inferior joint space. A hole was carefully drilled at the front junction of

the zygomatic arch with a 0.8 mm round bur. Orthodontic elastic bands (1/8 3.5oz, 3M Unitek, USA) were used to draw the disc forward. One end of the elastic band was attached to a 5-0 nylon suture, which penetrated through the anterior band of the disc. Then the other end was then attached to the hole. By elongating the elastic band from 3 mm to 10 mm, a tension force of 1 N was generated to stretch the disc anteriorly. The wound was thoroughly irrigated with saline and closed in layers with a 5-0 nylon sutures.

Postoperatively, animals received intramuscular antibiotics for 3 days. No notable differences in diet or weight were observed between groups, and all animals survived the study period. Five weeks after surgery, pigs were euthanized via bloodletting under deep anesthesia. Rats were also sacrificed five weeks after surgery. Subsequent gross examination confirmed the anterior disc displacement of the disc in the ADD group specimens.

Single-cell digestion and sequencing

First, we dissected the disc and retrodiscal tissue from the condyle. Next, tissues at the size of 5×5×5 mm^3 were cut from the intermediate region of the disc (disc sample) and retrodiscal tissue near the posterior band (retrodiscal tissue sample). Specimens were cut into small pieces (2-3 mm), then digested with 4 mg/ml Pronase (Roche, Switzerland) for 1 h, followed by digesting with 2 mg/ml Collagenase P (Roche, Switzerland) in fetal bovine serum (FBS)-free high glucose Dulbecco's modified eagle medium (DMEM) (Gibco, USA) for 2 h. After filtering with 70 μm and 40 μm filters,

the cell suspension was loaded into the 10X Chromium Single Cell Platform (10X Genomics). Generation of gel beads in emulsion (GEMs), barcoding, GEM-RT clean-up, complementary DNA amplification and library preparation and quantification were all performed according to the manufacturer's protocol (Single Cell 3′ library and Gel Bead Kit v.3). The final library pool was sequenced on the Illumina Hiseq sequencing systems.

Quality control of single-cell RNA sequencing data

This study included single-cell RNA sequencing (scRNA-seq) data from porcine-derived samples ('SHAM D', 'ADD D', 'CADD D', 'SHAM RT', 'ADD RT' and 'CADD RT'), which were processed using the Seurat R package (v4.0.5). The raw gene expression matrices were obtained from Cell Ranger output directories and imported using the 'Read10X' function. For each sample, a Seurat object was created with the 'CreateSeuratObject' function, and basic quality control metrics such as gene count distributions were initially assessed using basic R functions (e.g., 'summary', 'dim').

To further eliminate low-quality cells, we calculated the proportion of mitochondrial gene expression (e.g., *ND1*, *ND2*, *COX1*, *CYTB*) for each cell based on a curated mitochondrial gene list, and retained only cells with < 10% mitochondrial gene content ('percent.mt'). Furthermore, outlier cells were identified and removed using the Median Absolute Deviation (MAD) method applied to the log10-transformed total UMI counts ('nCount_RNA') and the number of detected genes ('nFeature_RNA'). Cells outside the median ± 3 × MAD range were excluded. At the gene level, following cell-level quality

control, we reconstructed the expression matrix by retaining only genes expressed in at least two cells ('min.cells = 2') to filter out low-abundance or biologically irrelevant noise genes.

Preprocessing and integration of single-cell RNA sequencing data

Each Seurat object was independently normalized using the 'NormalizeData' function. Highly variable genes were identified using the variance-stabilizing transformation (VST) method via 'FindVariableFeatures', with the top 2,000 most variable genes selected for downstream integration. To correct for batch effects and merge the datasets, we employed the canonical correlation analysis (CCA)-based integration pipeline in Seurat. Specifically, the 'FindIntegrationAnchors' function was used to identify anchor pairs across samples using the top 15 principal components (PCs), and the 'IntegrateData' function was then applied to generate a batch-corrected, integrated Seurat object.

Clustering, annotation and trajectory analysis of single-cell RNA sequencing data

The integrated dataset was subjected to dimensionality reduction, clustering, and differential gene expression (DGE) analysis using Seurat (v4.0.3.1). Clusters were manually annotated based on known marker genes of cell types (supplemental Figure 1D). Specific cell populations such as fibroblasts (FBs) and mural cells (MCs) were extracted for refined subclustering and re-annotation based on established literature. Functional enrichment analysis of marker gene lists was conducted using Metascape

for Gene Ontology (GO) term interpretation. Cell-cell communication analysis was performed using CellChat (v1.5.0), and trajectory inference was conducted using Monocle (v2.30.1) and CytoTRACE (v0.3.3).

Histological evaluation

Dissected specimens were fixed in 4% paraformaldehyde (PFA) (pH 7.4, Servicebio, China) at room temperature overnight, then embedded in paraffin after dehydration, and sectioned into 5 μm thick slices. Condyle samples were decalcified with 0.5 M EDTA (pH 7.2, Servicebio, China) for 3 months before embedding. Representative sections were stained with Hematoxylin-Eosin (H&E) (Fdbio science, China), Alcian Blue staining (Beyotime, China) and Safranin O and Fast Green staining (SO/FG) (Solarbio, China) according to the manufacturer's instructions. The Safranin-O positive area was calculated with ImageJ software (version 1.54). Modified Mankin score was used for evaluation of osteoarthritis severity according to previous study (79).

Identification of drug target

To identify key factors driving fibroblast remodeling, we combined a causal-inspired approach (P-NET) with a correlation-based approach (Seurat). This enabled us to identify high-confidence candidate targets that are both statistically correlated and biologically interpretable.

The P-NET algorithm integrates prior biological knowledge by embedding known gene to pathway relationships, enabling both prediction and interpretability of the deep

learning model (51). We used the gene expression profiles of fibroblasts from different groups as input features, and aggregated genes into corresponding pathway nodes according to Reactome annotations. These pathway nodes constituted a sparse feedforward intermediate layer. The model was trained using cross-validation and L1/L2 regularization to prevent overfitting and enhance generalizability. For model interpretability, we applied DeepLIFT (Deep Learning Important FeaTures) to compute feature importance scores, quantifying each gene's contribution to the model's predictions. Scores from different cross-validation folds were aggregated to generate a final gene-level ranking. Highly ranked genes were defined as P-NET selected features, representing upstream regulatory nodes that may have causal significance at the pathway level.

In parallel, we employed Seurat to perform differential expression analysis (DEG) of fibroblasts between different groups. This approach emphasizes statistical significance of expression changes and reveals transcriptional features associated with fibroblast remodeling from a data-driven perspective.

Next, the top 150 up- and down-regulated DEGs of fibroblasts between different groups were submitted to the Connectivity Map (CMap) for drug-response prediction, and complementary drug to gene interaction information was retrieved from DGIdb to construct a refined, data-driven drug database. By intersecting P-NET identified genes and Seurat-derived DEGs with target genes included in this database, we obtained a set of candidate target genes and corresponding small-molecule compounds potentially capable of modulating fibroblast function.

Isolation of primary porcine fibroblasts, mural cells and cell culture

TMJ retrodiscal tissue were separated from 5-month-old female mini pigs under aseptic conditions and rinsed with phosphate buffered saline (PBS) (Servicebio, China) to remove blood and other impurities. Tissue sample was then cut into approximately 1 mm^3 sections and digested in 4mg/ml Pronase for 1 h, followed by digesting in 2mg/ml Collagenase P in FBS-free DMEM for 2 h at 37℃. An equivalent volume of medium containing 10% FBS (Gibco, USA) was added to terminate the reaction. Cells were pelleted by centrifugation at 1000 rpm for 5 min. After removing the supernatant, cell pellet was resuspended with DMEM containing 10% FBS and 1% penicillin/streptomycin (Cienry, China).

Primary fibroblasts display robust adhesive properties and replicated relatively quickly. For enrichment of primary fibroblasts, we cultured cell suspension for 4 hours and adherent cells were collected and then passaged for several times to enrich fibroblasts (80). Additionally, unattached fractions of the cell suspension after the first 4 hours culture were transferred into new dishes to selectively enrich for mural cells. Mural cells, especially pericytes, can proliferate in media with lower concentrations of glucose and fetal bovine serum (81, 82). Therefore, the growth of endothelial cells and fibroblasts could be effectively inhibited in this nutrient media. After stable adhesion of cells, the complete medium was replaced by porcine pericyte complete medium (Procell, China).

Cells were cultured in a humidified incubator at 37°C and 5% CO_2. The medium was

completely changed every 3–4 days. When the cultures reached 70-80% confluence, the cells were subcultured using 0.25% trypsin-EDTA (Cienry, China). Cells at passage 3 were used in the following experiments.

Chondrogenic induction

Chondrogenic induction media was composed of DMEM supplemented with 10^{-7} mol dexamethasone (Sigma, USA), 1 mM sodium pyruvate (Sigma, USA), 50 μg/ml L-ascorbic-2-phosphate (Sigma, USA), 40 μg/ml L-proline (Sigma, USA), 1% insulin, transferrin, selenium (ITS, Beyotime, China), and 10 ng/ml TGF-β3 (PeproTech, USA).

Cells cultured in 6-well cell culture plate (Nest, China) underwent chondrogenic induction for 3 days and 7 days for qRT-PCR and WB analysis, respectively. For pellet culture, cells were first centrifuged for 5min at 300 g to form a pellet. After 3 weeks of chondrogenic induction, pellets were fixed in 4% paraformaldehyde and prepared for paraffin sections and were stained with Alcian Blue (Beyotime, China).

Immunofluorescence staining

Paraffin sections were deparaffinization and then performed antigen retrieval using 0.1% trypsin-EDTA for 30 min at 37℃. Subsequently, sections were blocked with PBST (PBS+ 0.1% Tween 20) supplied with 10% goat serum for 1 h at 37℃, then incubated with primary antibodies (ACTA2, 1:200, 67735-1-Ig, Proteintech, China; DCN, 1:50, PSH12-99, HuaBio, China; Aggrecan, 1:100, A11691, Abclonal, China; Collagen type II, 1:100, 28459-1-AP, Proteintech, China; SOX9, 1:100, ab185966,

Abcam, UK; FGF2 1:100, BD-PT5549, Biodragon, China; BMP5 1:100, PK10384, Abmart, China; Ki67 1:100, 27309-1-AP, Proteintech, China; COL1A1 1:200, HA722517, HuaBio, China; APOE, 1:100, 66830-1-Ig, Proteintech, China) overnight at 4℃. Sections were incubated with the secondary antibodies for 1 h at 37℃ (goat anti-mouse Alexa Fluor 488, HA1125; goat anti-rabbit Alexa 594, HA1122; 1:500, HuaBio, China). Slices were mounted with Antifade Mounting Medium with DAPI (Solarbio, China) and detected by laser scanning confocal microscopy (Pannoramic 250 FLASH, 3DHISTECH, Hungary). Three area were randomly selected to calculate percentages of Aggrecan^{+} area, Collagen type II^{+} area and SOX9^{+} cells using ImageJ software (version 1.54).

Primary porcine fibroblasts were collected and resuspended in 35mm confocal dishes (Nest, China) and incubated for two days. Cells were fixed in 4% paraformaldehyde (PFA) in PBS (pH 7.4, Servicebio, China) for 15 min at room temperature. After washing with ice-cold PBS for three times, cells were then permeabilized with 0.1% Triton X-100 (Beyotime, China) for 10 min. After washing, cells were incubated with 3% BSA in PBST (PBS+ 0.1% Tween 20) for 1 h at 37℃ to block unspecific binding of the antibodies. After decanting the solution, cells were further incubated with diluted primary antibody (APOE, 1:100, 66830-1-Ig, Proteintech, China; COL1A1, 1:100, HA722517, HuaBio, China; Smad4, 1:100, ET1604-12, HuaBio, China; ACTA2, 1:200, 67735-1-Ig, Proteintech, China) in 3% BSA in PBST overnight at 4℃, then incubated with diluted secondary antibody (goat anti-mouse Alexa Fluor 488, HA1125; goat anti-rabbit Alexa 594, HA1122; 1:500, HuaBio, China) in 3% BSA in PBST for 1 h at 37℃.

Cells were stained with DAPI (Solarbio, China) for 5 min at room temperature and washed with PBS for three times, then observed under microscope (LSM 980, Zeiss, Germany).

RNA isolation and quantitative real time PCR (qRT-PCR)

Total RNA of fibroblasts was purified with RNAeasy™ Animal RNA Isolation Kit with Spin Column (Beyotime, China). RNA quantity and purity were determined using Nanodrop OneC (Thermo scientific, USA). RNA samples (260/280 ≥ 1.8) were used to obtain cDNA with HiScript III RT SuperMix for qPCR (Vazyme, China). QRT-PCR was performed using ChamQ Universal SYBR qPCR Master Mix (Vazyme, China). Primers for RT-qPCR were listed in Supplemental Table 1. Each sample was run in triplicate to ensure quantitative accuracy. The results were calculated using the $2^{-\Delta\Delta Ct}$ method. Gene expression levels were normalized to the housekeeping gene Glyceraldehyde 3-phosphate dehydrogenase (*GAPDH*).

Western blot

Cells were collected and lysed in 1× protein loading buffer containing DTT, and boiled at 95℃ for 10 min. Proteins were resolved by SDS-PAGE and transferred to polyvinylidene difluoride membranes. After blocked in 5% skimmed milk in tris-buffered saline with 0.1% Tween 20 (TBST) for 1 h at room temperature, membranes were cut and incubated with diluted primary antibodies overnight at 4℃. The primary antibodies included FN1 (1:1000, T59537, abmart, China), COL1A1 (1:1000,

HA722517, HuaBio, China), DCN (1:1000, HA723504, HuaBio, China), ACTA2 (1:1000, 67735-1-Ig, Proteintech, China), FGF2 (1:1000, BD-PT5549, Biodragon, China), BMP5 (1:1000, PK10384, Abmart, China), Aggrecan (1:1000, A11691, Abclonal, China), Collagen type II (1:1000, 28459-1-AP, Proteintech, China), SOX9 (1:1000, ab185966, Abcam, UK), Phospho-Smad1/5/9 (1:1000, HA722566, HuaBio, China), Smad1/5/9 (1:1000, ER64980, HuaBio, China), Phospho-ERK1/2 (1:1000, 28733-1-ap, Proteintech, China), ERK1/2 (1:5000, 51068-1-ap, Proteintech, China) and GAPDH (1:10000, 60004-1-Ig, Proteintech, China). Then membranes were incubated with diluted HRP conjugated goat anti-rabbit or anti-mouse secondary antibodies (1:10000, HA1001, HA1006, HuaBio, China) for 1 h at room temperature. Finally, enhanced chemiluminescence detection reagents (Fdbio science, China) were used to scan membranes in the imaging system (Bio-Rad ChemiDoc MP, USA).

Micro-computed tomography (micro-CT) scanning, reconstruction and microstructural analysis

The TMJ specimens were scanned with a high-resolution micro-CT system (SkyScan1276, Bruker, Belgium). Scanning was performed at a source voltage of 60 kV, a current of 200 μA, with a 0.5-mm aluminum filter and the voxel size was 13 μm. Images were acquired with 2 × 2 camera binning, exposure time 229 ms. Scanning was performed in step-and-shoot mode with flat-field correction and random movement disabled. The raw projection images were reconstructed using NRecon (version 2.2.0.6). A region of interest (ROI) was defined within the trabecular bone area, excluding the

cortical shell. The following standard bone morphometric parameters were calculated using CTAn software (Bruker) according to the guidelines (83): BV/TV (%): Bone volume fraction (bone volume/total volume), Tb.Th (μm): Trabecular thickness, Tb.Sp (μm): Trabecular spacing, Tb.N (1/mm): Trabecular number. All morphometric parameters were calculated using a 3D model-independent method based on distance transformation algorithms as implemented in CTAn. Three-dimensional visualization of the bone structure was performed using CTVol software (Bruker).

Statistics

All statistical analyses were performed with R (version 4.3) and PRISM (GraphPad Software, version 9.0). Data are presented as the means ± standard deviation (SD). Comparisons between two groups were performed using unpaired, 2-tailed Student's *t* test. For multiple group comparisons, one-way ANOVA followed by Tukey's honestly significant difference (HSD) post hoc test or Kruskal-Wallis test followed by Dunn's multiple comparisons test. A *P* value less than 0.05 was considered statistically significant.

Study approval

The study protocols were reviewed and approved by the Animal Ethics Committee of Zhejiang Chinese Medical University, China (approval No.20230227-08). All procedures were conducted in strict accordance with the Guidelines for Animal Care and Use Standards.

692

693 **Data availability**

694 All data supporting the findings of this study are included in the article supplemental
695 data and supporting data values, or are available from the corresponding authors upon
696 reasonable request. Sequencing data have been deposited in the Genome Sequence
697 Archive in National Genomics Data Center, China National Center for Bioinformation
698 (accession number: CRA034150).

699

Author contributions

WY designed the study, performed animal and cell experiments, acquired data, analyzed data, drafted the manuscript and revised the manuscript. YC designed the study, performed animal and cell experiments, analyzed data, drafted the manuscript and revised the manuscript. RY performed bioinformatics analysis, analyzed data, supported the interpretation of results and revised the manuscript. WL performed animal experiments and acquired data. CW analyzed data and assisted in animal model validation. YW and QD participated in data collection. WL and MZ critically reviewed the manuscript. XC supervised the study and critically reviewed the manuscript. JS supervised the study, provided reagents for animal and cell experiments and critically reviewed the manuscript.

Acknowledgments

This work was supported by the grants from the National Natural Science Foundation of China (82170984), the National Traditional Chinese Medicine Comprehensive Reform Demonstration Zone Science and Technology Cooperation Project (GZY-KJS-ZJ-2025-094) and it was a project supported by Scientific Research Fund of Zhejiang University (XY2024036).

We thank Huang Qiong, Chen Jingyao from the Core Facilities, Zhejiang University School of Medicine for their technical support.

References

1. Valesan LF, et al. Prevalence of temporomandibular joint disorders: a systematic review and meta-analysis. Clinical oral investigations. 2021;25(2):441-453.

2. Katzberg RW, Tallents RH. Normal and abnormal temporomandibular joint disc and posterior attachment as depicted by magnetic resonance imaging in symptomatic and asymptomatic subjects. Journal of oral and maxillofacial surgery : official journal of the American Association of Oral and Maxillofacial Surgeons. 2005;63(8):1155-1161.

3. Takaoka R, et al. Relative risk of positional and dynamic temporomandibular disc abnormality for osteoarthritis-magnetic resonance imaging study. Journal of oral rehabilitation. 2021;48(4):375-383.

4. Sener S, Akgänlü F. MRI characteristics of anterior disc displacement with and without reduction. Dento maxillo facial radiology. 2004;33(4):245-252.

5. Peroz I, et al. MRI of the TMJ: morphometric comparison of asymptomatic volunteers and symptomatic patients. Quintessence international (Berlin, Germany : 1985). 2011;42(8):659-667.

6. Willard VP, et al. The attachments of the temporomandibular joint disc: a biochemical and histological investigation. Archives of oral biology. 2012;57(6):599-606.

7. Coombs MC, et al. Structure-Function Relationships of Temporomandibular Retrodiscal Tissue. Journal of dental research. 2017;96(6):647-653.

8. Machon V, et al. Temporomandibular joint disc perforation: a retrospective study. International journal of oral and maxillofacial surgery. 2017;46(11):1411-1416.

9. Nguyen NGK, et al. A rat model for inducing temporomandibular anterior disc displacement

742 experimentally. Journal of oral science. 2020;62(1):70-74.
743 10. Gu Z, et al. Type II collagen and aggrecan mRNA expression by in situ hybridization in rabbit
744 temporomandibular joint posterior attachment following disc displacement. Archives of oral
745 biology. 2003;48(1):55-62.
746 11. Bristela M, et al. Magnetic resonance imaging of temporomandibular joint with anterior disk
747 dislocation without reposition - long-term results. Clinical oral investigations. 2017;21(1):237-
748 245.
749 12. Blaustein DI, Scapino RP. Remodeling of the temporomandibular joint disk and posterior
750 attachment in disk displacement specimens in relation to glycosaminoglycan content. Plastic
751 and reconstructive surgery. 1986;78(6):756-764.
752 13. Luder HU. Articular degeneration and remodeling in human temporomandibular joints with
753 normal and abnormal disc position. Journal of orofacial pain. 1993;7(4):391-402.
754 14. Ruscitto A, et al. Evidence of vasculature and chondrocyte to osteoblast transdifferentiation in
755 craniofacial synovial joints: Implications for osteoarthritis diagnosis and therapy. FASEB
756 journal : official publication of the Federation of American Societies for Experimental Biology.
757 2020;34(3):4445-4461.
758 15. Kalpakci KN, et al. An interspecies comparison of the temporomandibular joint disc. Journal of
759 dental research. 2011;90(2):193-198.
760 16. Li H, et al. Disc positions and condylar changes induced by different stretching forces in the
761 model for anterior disc displacement of temporomandibular joint. The Journal of craniofacial
762 surgery. 2014;25(6):2112-2116.
763 17. Bi R, et al. A single-cell transcriptional atlas reveals resident progenitor cell niche functions in

TMJ disc development and injury. Nature communications. 2023;14(1):830.

18. Zhou T, et al. Spatiotemporal Characterization of Human Early Intervertebral Disc Formation at Single-Cell Resolution. Advanced science (Weinheim, Baden-Wurttemberg, Germany). 2023;10(14):e2206296.

19. Nakao Y, et al. Proteoglycan expression is influenced by mechanical load in TMJ discs. Journal of dental research. 2015;94(1):93-100.

20. DeLeon-Pennell KY, et al. Fibroblasts: The arbiters of extracellular matrix remodeling. Matrix biology : journal of the International Society for Matrix Biology. 2020;91-92:1-7.

21. Pufe T, et al. Pleiotrophin, an embryonic differentiation and growth factor, is expressed in osteoarthritis. Osteoarthritis and cartilage. 2003;11(4):260-264.

22. Quinn CM, et al. Induction of fibroblast apolipoprotein E expression during apoptosis, starvation-induced growth arrest and mitosis. The Biochemical journal. 2004;378(Pt 3):753-761.

23. Hasegawa A, et al. Role of Fibulin 3 in Aging-Related Joint Changes and Osteoarthritis Pathogenesis in Human and Mouse Knee Cartilage. Arthritis & rheumatology (Hoboken, NJ). 2017;69(3):576-585.

24. Posey KL, et al. Cartilage oligomeric matrix protein: COMPopathies and beyond. Matrix biology : journal of the International Society for Matrix Biology. 2018;71-72:161-173.

25. Zheng Z, et al. Fibromodulin, a Multifunctional Matricellular Modulator. Journal of dental research. 2023;102(2):125-134.

26. Sänger CS, et al. Serine protease 35 regulates the fibroblast matrisome in response to hyperosmotic stress. Science advances. 2023;9(35):eadh9219.

27. Waller KA, et al. Role of lubricin and boundary lubrication in the prevention of chondrocyte

apoptosis. Proceedings of the National Academy of Sciences of the United States of America. 2013;110(15):5852-5857.

28. Abreu-Velez AM, Howard MS. Collagen IV in Normal Skin and in Pathological Processes. North American journal of medical sciences. 2012;4(1):1-8.

29. Ezura Y, et al. Differential expression of lumican and fibromodulin regulate collagen fibrillogenesis in developing mouse tendons. The Journal of cell biology. 2000;151(4):779-788.

30. Richter A, et al. EGFL7 Mediates BMP9-Induced Sprouting Angiogenesis of Endothelial Cells Derived from Human Embryonic Stem Cells. Stem cell reports. 2019;12(6):1250-1259.

31. Salazar VS, et al. BMP signalling in skeletal development, disease and repair. Nature reviews Endocrinology. 2016;12(4):203-221.

32. Kodama J, et al. Apolipoprotein E is a marker of all chondrocytes in the growth plate resting zone. Bone research. 2025;13(1):31.

33. Janjanam J, et al. Matricellular Protein WISP2 Is an Endogenous Inhibitor of Collagen Linearization and Cancer Metastasis. Cancer research. 2021;81(22):5666-5677.

34. Xie L, et al. Cystatin C increases in cardiac injury: a role in extracellular matrix protein modulation. Cardiovascular research. 2010;87(4):628-635.

35. Gao Y, et al. Role of interferon alpha-inducible protein 6 in modulating the proliferation, apoptosis and senescence of oesophageal squamous cell carcinoma cells. Journal of physiology and pharmacology : an official journal of the Polish Physiological Society. 2023;74(3).

36. Lorda-Diez CI, et al. Apoptosis during embryonic tissue remodeling is accompanied by cell senescence. Aging. 2015;7(11):974-985.

37. He H, et al. Single-cell transcriptome analysis of human skin identifies novel fibroblast

subpopulation and enrichment of immune subsets in atopic dermatitis. The Journal of allergy and clinical immunology. 2020;145(6):1615-1628.

38. Zhang M, et al. Applications of stripe assay in the study of CXCL12-mediated neural progenitor cell migration and polarization. Biomaterials. 2015;72:163-171.

39. Siekmann AF. Biology of vascular mural cells. Development (Cambridge, England). 2023;150(16).

40. Alex L, et al. Cardiac Pericytes Acquire a Fibrogenic Phenotype and Contribute to Vascular Maturation After Myocardial Infarction. Circulation. 2023;148(11):882-898.

41. Crouch EE, et al. Ensembles of endothelial and mural cells promote angiogenesis in prenatal human brain. Cell. 2022;185(20):3753-3769.e3718.

42. Neumaier EE, et al. The role of midkine in health and disease. Frontiers in immunology. 2023;14:1310094.

43. Sun C, et al. Functions of exogenous FGF signals in regulation of fibroblast to myofibroblast differentiation and extracellular matrix protein expression. Open biology. 2022;12(9):210356.

44. Lorda-Diez CI, et al. Ligand- and stage-dependent divergent functions of BMP signaling in the differentiation of embryonic skeletogenic progenitors in vitro. Journal of bone and mineral research : the official journal of the American Society for Bone and Mineral Research. 2014;29(3):735-748.

45. Liu L, et al. TWEAK-Fn14 signaling protects mice from pulmonary fibrosis by inhibiting fibroblast activation and recruiting pro-regenerative macrophages. Cell reports. 2025;44(2):115220.

46. Morse C, et al. Proliferating SPP1/MERTK-expressing macrophages in idiopathic pulmonary

fibrosis. The European respiratory journal. 2019;54(2).

47. Djudjaj S, et al. Macrophage Migration Inhibitory Factor Limits Renal Inflammation and Fibrosis by Counteracting Tubular Cell Cycle Arrest. Journal of the American Society of Nephrology : JASN. 2017;28(12):3590-3604.

48. Kim J, et al. PDGF signaling is required for epicardial function and blood vessel formation in regenerating zebrafish hearts. Proceedings of the National Academy of Sciences of the United States of America. 2010;107(40):17206-17210.

49. Lee YJ, et al. Administration of Gas6 attenuates lung fibrosis via inhibition of the epithelial-mesenchymal transition and fibroblast activation. Cell biology and toxicology. 2024;40(1):20.

50. Dahl TB, et al. Visfatin/NAMPT: a multifaceted molecule with diverse roles in physiology and pathophysiology. Annual review of nutrition. 2012;32:229-243.

51. Elmarakeby HA, et al. Biologically informed deep neural network for prostate cancer discovery. Nature. 2021;598(7880):348-352.

52. Lalmanach G, et al. Human cystatin C in fibrotic diseases. Clinica chimica acta; international journal of clinical chemistry. 2025;565:120016.

53. Chen J, et al. FGL1 and FGL2: emerging regulators of liver health and disease. Biomarker research. 2024;12(1):53.

54. Zou L, et al. Analysis of joint protein expression profile in anterior disc displacement of TMJ with or without OA. Oral diseases. 2024;30(7):4463-4482.

55. Holch A, et al. Respiratory ß-2-Microglobulin exerts pH dependent antimicrobial activity. Virulence. 2020;11(1):1402-1414.

56. Corbel M, et al. Inhibition of bleomycin-induced pulmonary fibrosis in mice by the matrix

metalloproteinase inhibitor batimastat. The Journal of pathology. 2001;193(4):538-545.

57. Li YY, Feldman AM. Matrix metalloproteinases in the progression of heart failure: potential therapeutic implications. Drugs. 2001;61(9):1239-1252.

58. Goodman VL, et al. Approval summary: sunitinib for the treatment of imatinib refractory or intolerant gastrointestinal stromal tumors and advanced renal cell carcinoma. Clinical cancer research : an official journal of the American Association for Cancer Research. 2007;13(5):1367-1373.

59. Sourdon J, et al. Sunitinib-induced cardiac hypertrophy and the endothelin axis. Theranostics. 2021;11(8):3830-3838.

60. Gupta RA, et al. GPR35 agonists inhibit TRPA1-mediated colonic nociception through suppression of substance P release. Pain. 2025;166(3):596-613.

61. Sekut L, et al. Anti-inflammatory activity of phosphodiesterase (PDE)-IV inhibitors in acute and chronic models of inflammation. Clinical and experimental immunology. 1995;100(1):126-132.

62. Sato S, et al. Natural course of nonreducing disc displacement of the temporomandibular joint: changes in chewing movement and masticatory efficiency. Journal of oral and maxillofacial surgery : official journal of the American Association of Oral and Maxillofacial Surgeons. 2002;60(8):867-872.

63. Liu XM, et al. Correlation between disc displacements and locations of disc perforation in the temporomandibular joint. Dento maxillo facial radiology. 2010;39(3):149-156.

64. Zhou J, et al. Comparing microstructural and micromechanical deformation of the TMJ disc in two anterior disc displacement models. Journal of oral rehabilitation. 2024;51(11):2390-2397.

65. Meng XM, et al. TGF-β: the master regulator of fibrosis. Nature reviews Nephrology. 2016;12(6):325-338.

66. Feng H, et al. Tendon-derived cathepsin K-expressing progenitor cells activate Hedgehog signaling to drive heterotopic ossification. The Journal of clinical investigation. 2020;130(12):6354-6365.

67. Bechtold TE, et al. Excess BMP Signaling in Heterotopic Cartilage Forming in Prg4-null TMJ Discs. Journal of dental research. 2016;95(3):292-301.

68. Miyahara J, et al. CD34hi subset of synovial fibroblasts contributes to fibrotic phenotype of human knee osteoarthritis. JCI insight. 2025;10(2).

69. Zhu D, et al. Wedelolactone Enhances Osteoblastogenesis through ERK- and JNK-mediated BMP2 Expression and Smad/1/5/8 Phosphorylation. Molecules (Basel, Switzerland). 2018;23(3).

70. Liu X, et al. SMAD4, activated by the TCR-triggered MEK/ERK signaling pathway, critically regulates CD8(+) T cell cytotoxic function. Science advances. 2022;8(30):eabo4577.

71. Shih HY, et al. Bmp5 Regulates Neural Crest Cell Survival and Proliferation via Two Different Signaling Pathways. Stem cells (Dayton, Ohio). 2017;35(4):1003-1014.

72. Huyut Z, et al. Can zaprinast and avanafil induce the levels of angiogenesis, bone morphogenic protein 2, 4 and 7 in kidney of ovariectomised rats? Archives of physiology and biochemistry. 2022;128(4):945-950.

73. Yang J, et al. Sildenafil potentiates bone morphogenetic protein signaling in pulmonary arterial smooth muscle cells and in experimental pulmonary hypertension. Arteriosclerosis, thrombosis, and vascular biology. 2013;33(1):34-42.

74. Li G, et al. Mechanical compressive force inhibits adipogenesis of adipose stem cells. Cell proliferation. 2013;46(5):586-594.

75. Marangoni RG, et al. Adipocytic Progenitor Cells Give Rise to Pathogenic Myofibroblasts: Adipocyte-to-Mesenchymal Transition and Its Emerging Role in Fibrosis in Multiple Organs. Current rheumatology reports. 2020;22(11):79.

76. Trayhurn P. Hypoxia and adipose tissue function and dysfunction in obesity. Physiological reviews. 2013;93(1):1-21.

77. Bueno CH, et al. Gender differences in temporomandibular disorders in adult populational studies: A systematic review and meta-analysis. Journal of oral rehabilitation. 2018;45(9):720-729.

78. Polcari AJ, et al. Effect of the phosphodiesterase-5 inhibitor zaprinast on ischemia-reperfusion injury in rats. Journal of endourology. 2013;27(3):338-342.

79. He Y, et al. AB0104 Develop and Evaluate a New Modified Mankin Score System with Special Attention to Subchondral Bone. Annals of the Rheumatic Diseases. 2014;73:838.

80. Bravo JI, et al. Protocol for isolation of adult mouse ear pinnae-derived primary fibroblasts. STAR protocols. 2021;2(2):100406.

81. Hariharan A, et al. Brain capillary pericytes are metabolic sentinels that control blood flow through a K(ATP) channel-dependent energy switch. Cell reports. 2022;41(13):111872.

82. Tang L, et al. Isolation and characterization of peritoneal microvascular pericytes. FEBS open bio. 2022;12(4):784-797.

83. Bouxsein ML, et al. Guidelines for assessment of bone microstructure in rodents using micro-computed tomography. Journal of bone and mineral research : the official journal of the

918 American Society for Bone and Mineral Research. 2010;25(7):1468-1486.

Figure legends

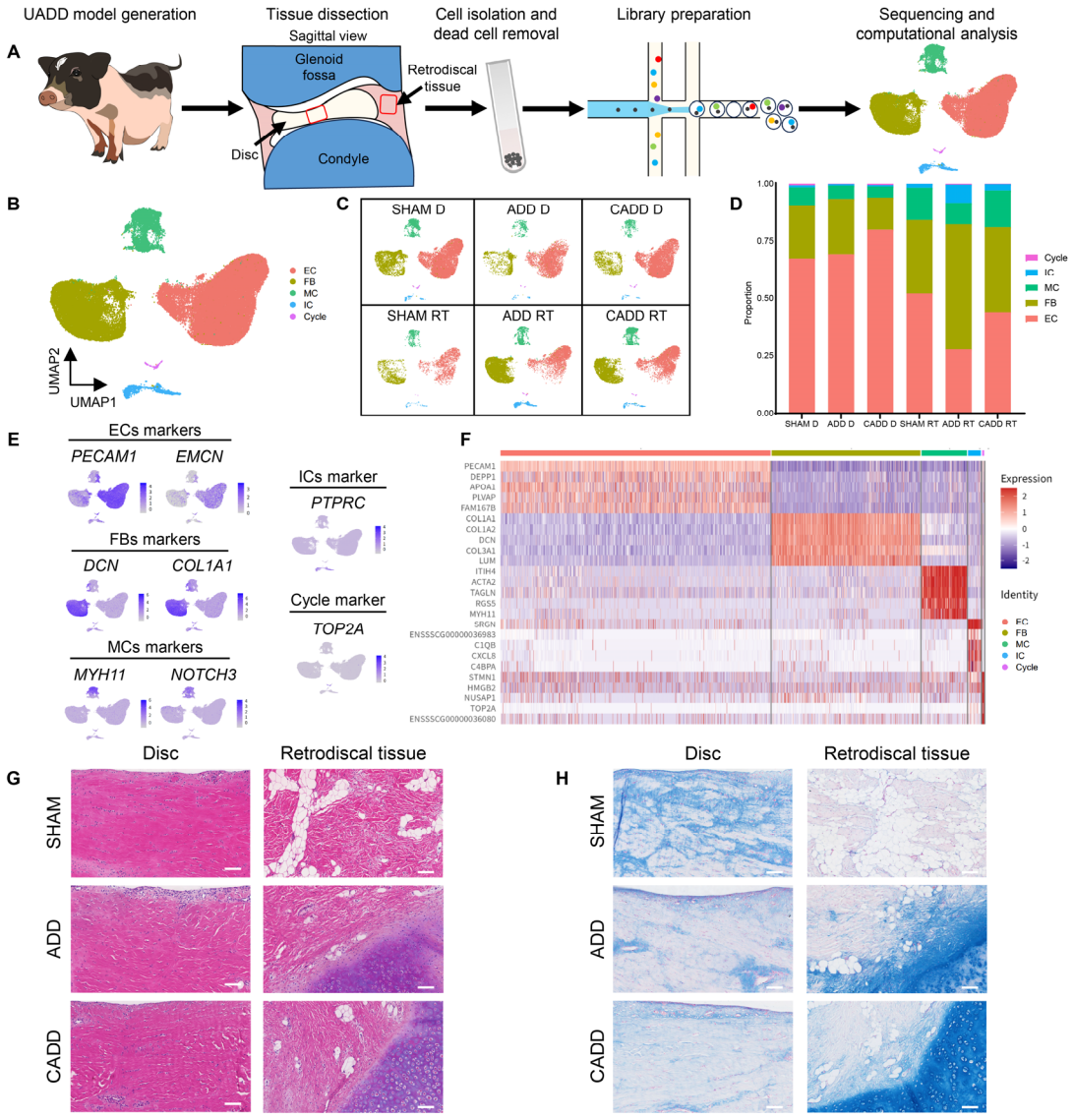

Figure 1. The cellular landscape and histological features of porcine TMJ discs and retrodiscal tissues from SHAM, ADD and CADD groups. (**A**) A schematic workflow illustrating the generation of the UADD pig model and subsequent dissection of pig TMJ discs and retrodiscal tissues for single-cell transcriptomic analysis. (**B**) Dimension reduction presentation of combined single-cell transcriptome data from TMJ discs and retrodiscal tissues of all groups. Each dot represents a single-cell and is labeled with corresponding cell categories and colored according to

its cell type identity. Five cell clusters are visualized by a uniform manifold approximation and projection (UMAP) plot: endothelial cells (ECs); fibroblasts (FBs); immune cells (ICs); mural cells (MCs); cells in cell cycle (Cycle). (**C**) Dimension reduction presentation of single-cell transcriptome data of TMJ discs and retrodiscal tissues from SHAM, ADD and CADD groups via UMAP, displayed separately by tissue origins and groups. (**D**) Bar graph shows the fraction of cell clusters by tissue origins and groups. (**E**) Expression patterns of selected markers projected on the UMAP plot. (**F**) Heatmap revealing the top 5 differentially expressed genes (DEGs) of each cell cluster. Representative hematoxylin-eosin (H&E) staining (**G**) and alcian blue staining (**H**) of the TMJ discs and retrodiscal tissues from SHAM, ADD and CADD groups. Scale bars: 100 μm.

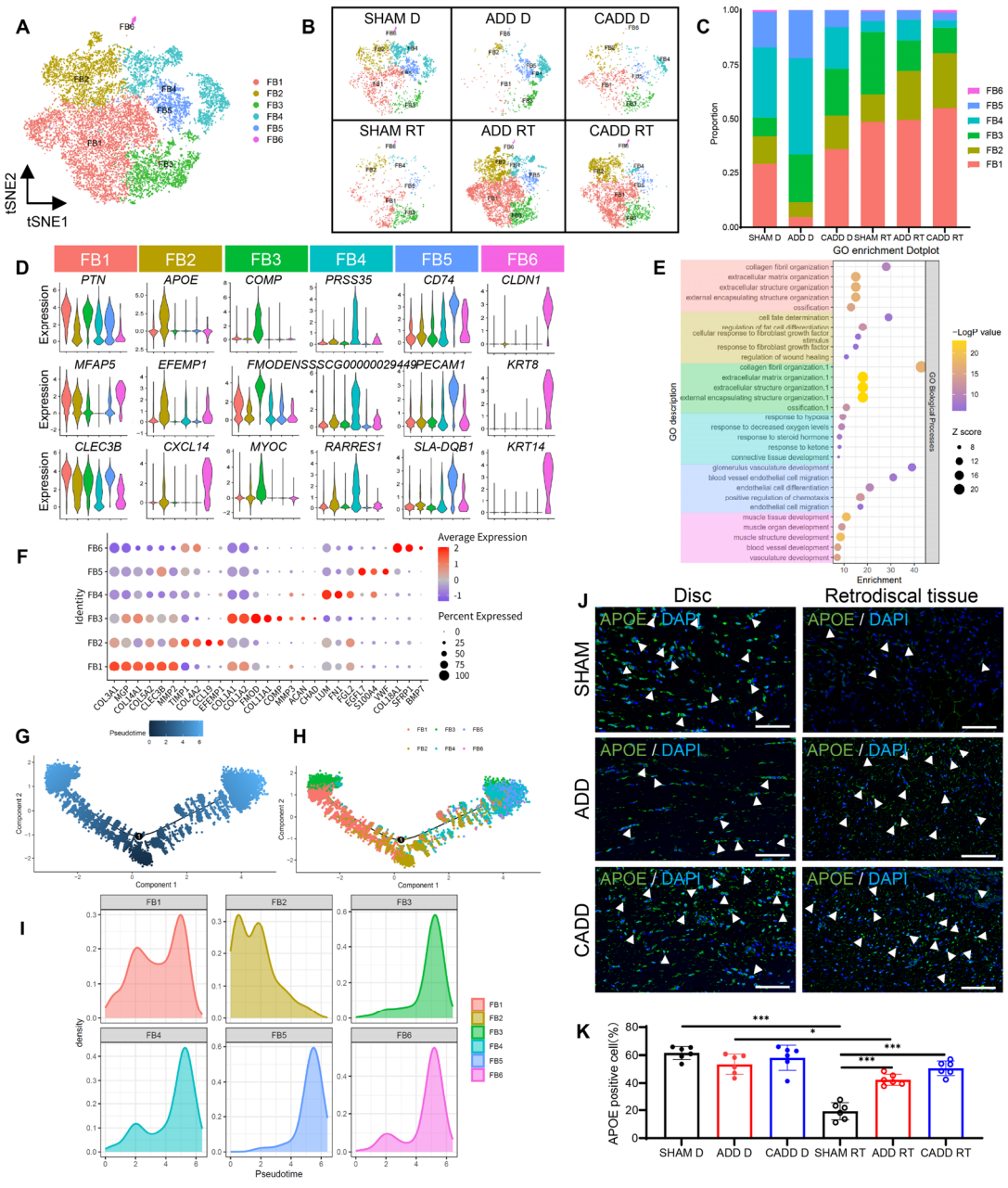

Figure 2. Characterization of fibroblast subtypes participating in adaptive remodeling of the retrodiscal tissue. (**A**) Dimension reduction presentation of combined single-cell transcriptome data of fibroblast (FB) cluster from TMJ discs and retrodiscal tissues of all groups. Six subclusters of fibroblasts are identified and visualized by a t-distributed stochastic neighbor embedding (t-SNE) plot. (**B**) Dimension reduction presentation of single-cell transcriptome data of FB cluster in SHAM, ADD and CADD groups from TMJ discs and retrodiscal tissues via t-SNE, displayed separately by tissue origins and groups. (**C**) Bar graph shows the fraction of FB subclusters by tissue origins and

groups. (**D**) Violin plots show the expression of differentially expressed genes (DEGs) in different FB subclusters. Expression values are normalized. (**E**) Dot plot of Gene Ontology (GO) Biological Process enrichment analysis of DEGs in different FB subclusters. (**F**) Expression of extracellular matrix (ECM) markers in different FB clusters. Monocle analysis shows the trajectory order of FBs colored by pseudotime value (**G**) and cell type (**H**). (**I**) Density distribution of FB subclusters along pseudotime. (**J**) Representative images of TMJ discs and retrodiscal tissues subjected to immunofluorescence staining for APOE in different groups and quantification (**K**), three random fields were selected from each of the two pig samples for measurement. Statistical significance was determined by 1-way ANOVA. Data represent mean ± SD. $*P < 0.05$, $***P < 0.001$. Green: APOE; Blue: DAPI; White arrowhead: Cells expressing APOE. Scale bars: 100 μm.

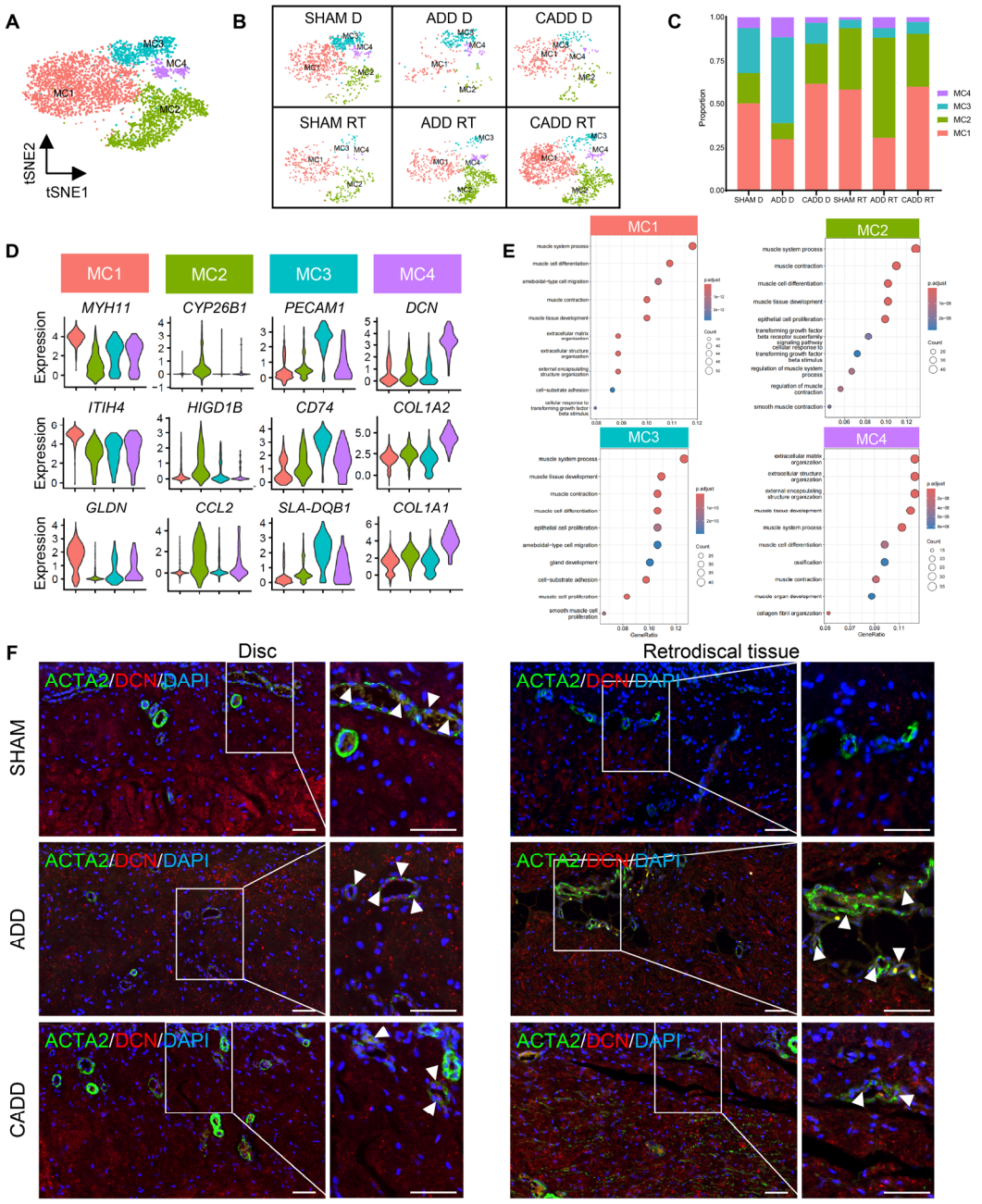

Figure 3. Identification of a specific ECM-related mural cell subcluster in the retrodiscal tissue after ADD induction. (**A**) Dimension reduction presentation of combined single-cell transcriptome data of mural cell (MC) cluster from TMJ disc and retrodiscal tissues of all groups. Four subclusters of mural cells are identified and visualized by a t-distributed stochastic neighbor embedding (t-SNE) plot. (**B**) Dimension reduction presentation of single-cell transcriptome data of MC cluster in SHAM, ADD and CADD groups from TMJ disc and retrodiscal tissues via t-SNE, displayed separately by

tissue origins and groups. (**C**) Bar graph shows the fraction of MC subtypes by tissue origins and groups. (**D**) Violin plots show the expression of differentially expressed genes (DEGs) in different MC subclusters. Expression values are normalized. (**E**) Dot plot of Gene Ontology (GO) Biological Process enrichment analysis of DEGs in different MC subclusters. (**F**) Representative images of TMJ discs and retrodiscal tissues subjected to immunofluorescence staining for ACTA2 and DCN in different groups, three random fields were selected from each of the two pig samples. Green: ACTA2; Red: DCN; Blue: DAPI; White arrowhead: Cells co-expressing of ACTA2 and DCN. Scale bars: 50 μm.

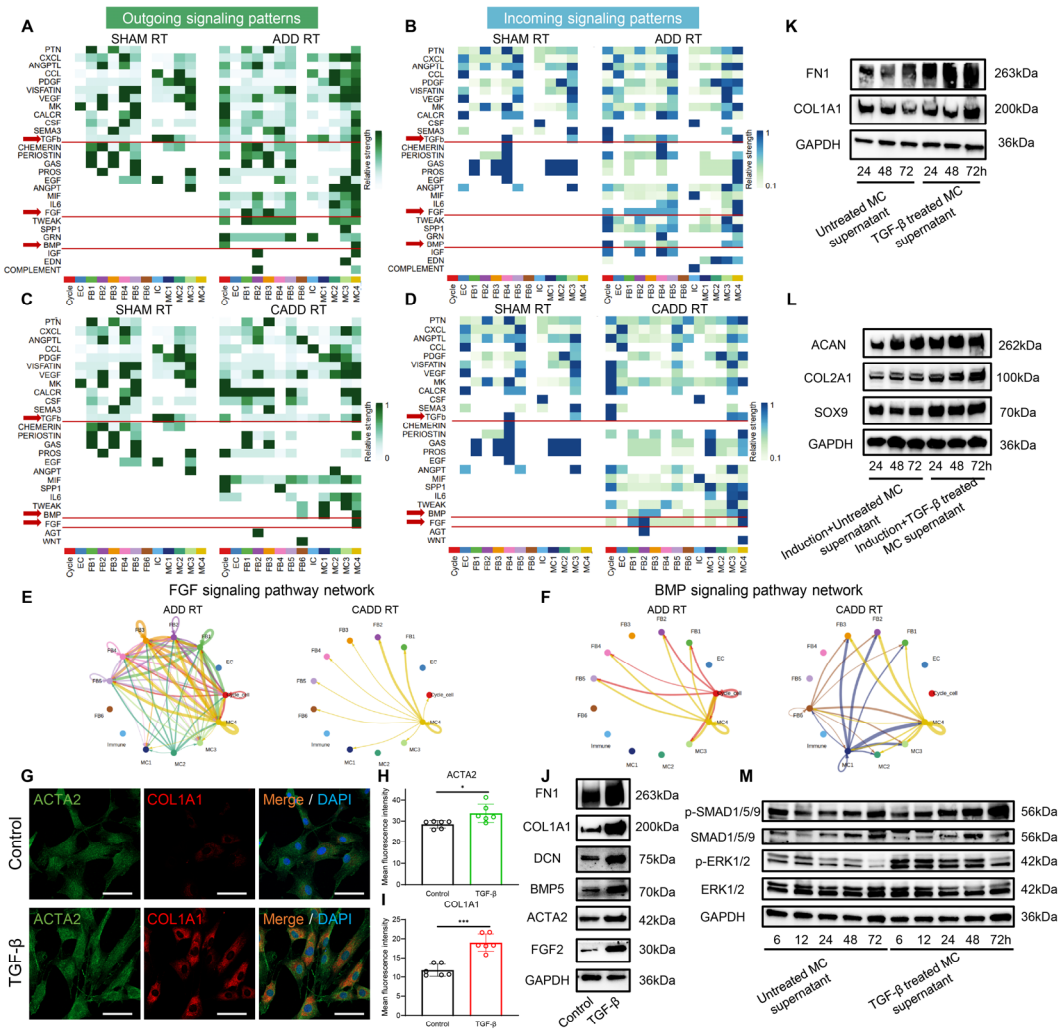

Figure 4. FGF and BMP signaling pathways are involved in adaptive remodeling of the retrodiscal tissue. Heatmap of outgoing signaling pathways in different cell clusters in SHAM and ADD RT groups (**A**), SHAM and CADD RT groups (**C**). Heatmap of incoming signaling pathways in different cell clusters in SHAM and ADD RT groups (**B**), SHAM and CADD RT groups(**D**). The inferred FGF signaling pathway (**E**) and BMP5 signaling pathway (**F**) networks in ADD and CADD RT groups. Edge width represents the communication probability between cell types. (**G**) Immunofluorescence staining for ACTA2 and COL1A1 in mural cells (MCs) and quantification (**H**, **I**) (n=6). Statistical significance was determined by Student's *t* test. Data represent mean ± SD. $*P < 0.05$, $***P < 0.001$. Green: ACTA2; Red: COL1A1; Blue: DAPI. Scale bars: 50 μm. (**J**)

Evaluation of fibroblast and smooth muscle cell marker levels in mural cells. (**K**) Evaluation of fibrogenic protein levels in fibroblasts treated with different MC supernatants. (**L**) Evaluation of chondrogenic protein levels in fibroblasts treated with different MC supernatants under chondrogenic induction. (**M**) Evaluation of SMAD1/5/9 and ERK1/2 cascade activation in fibroblasts treated with different MC supernatants. For representative western blot, 3 replicates were conducted.

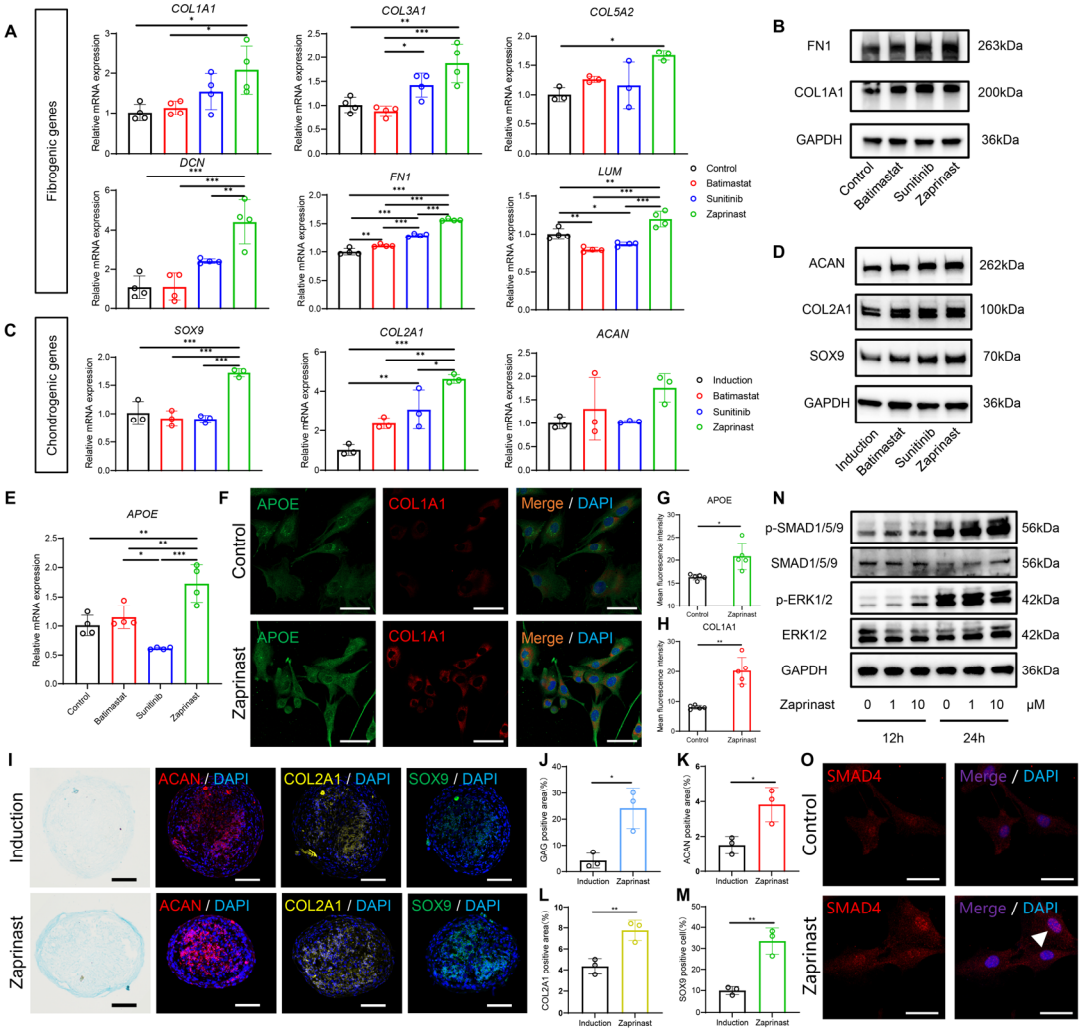

988

989 **Figure 5. Zaprinast exhibits most prominent pro-fibrotic and chondrogenic effects on**

990 **fibroblasts by ERK1/2 and SMAD1/5/9 cascade activation.** Evaluation of fibrogenic gene

991 expressions (**A**) and protein levels (**B**) treated with Batimastat, Sunitinib and Zaprinast. Evaluation

992 of chondrogenic gene expressions (**C**) and protein levels (**D**) treated with Batimastat, Sunitinib and

993 Zaprinast under chondrogenic induction. (**E**) Gene expression of *APOE* treated with Batimastat,

994 Sunitinib and Zaprinast. Fold changes were normalized with *GAPDH* (n=3-4). Statistical

995 significance was determined by 1-way ANOVA. Data represent mean ± SD. **P* < 0.05, ***P*< 0.01,

996 ****P* < 0.001. For representative western blot, 3 replicates were conducted. (**F**)

997 Immunofluorescence staining for APOE and COL1A1 in fibroblasts and quantification (**G**, **H**) (n=5).

998 Statistical significance was determined by Student's *t* test. Data represent mean ± SD. *$P < 0.05$,
999 **$P < 0.01$. Green: APOE; Red: COL1A1; Blue: DAPI. Scale bars: 50 μm. (**I**) Alcian blue staining,
1000 immunofluorescence staining of ACAN, COL2A1 and SOX9 of pellet and quantification (**J-M**)
1001 (n=3). Statistical significance was determined by Student's *t* test. Data represent mean ± SD.
1002 *$P < 0.05$, **$P < 0.01$. Red: ACAN; Yellow: COL2A1; Green: SOX9; Blue: DAPI. Scale bars: 100
1003 μm. (**N**) Evaluation of ERK1/2 and SMAD1/5/9 cascade activation in fibroblast treated with
1004 Zaprinast. For representative western blot, 3 replicates were conducted. (**O**) Immunofluorescence
1005 staining displays nuclear localization of SMAD4 in fibroblasts treated with Zaprinast (white
1006 arrowhead). Red: SMAD4; Blue: DAPI. For representative immunofluorescence staining of
1007 SMAD4, 3 replicates were conducted. Scale bars: 50 μm.

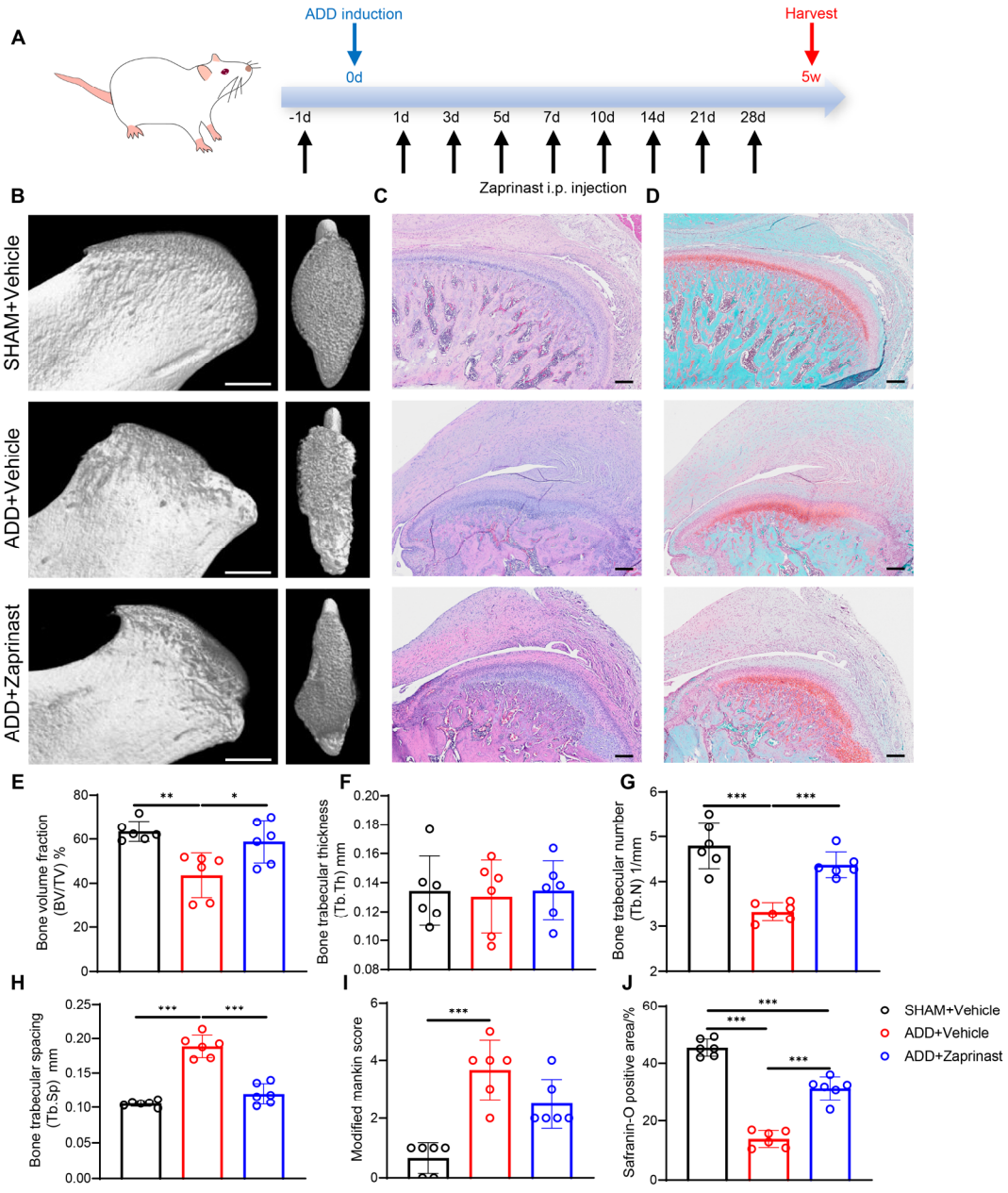

Figure 6. Zaprinast alleviates deformation of the disc and retrodiscal tissue and damage of condyle in vivo. (**A**) Timeline of ADD induction and Zaprinast administration in a rat model. (**B**) Representative 3D reconstruction images of condyle from SHAM+Vehicle, ADD+Vehicle and ADD+Zaprinast groups. Scale bars: 1 mm. (**C**) Hematoxylin and eosin (H&E) staining showing alteration in configuration of disc and retrodiscal tissue. Scale bars: 200 μm. (**D**) Safranin-O and fast green (SO/FG) staining showing changes in proteoglycan content. Scale bars: 200 μm. (**E-H**) Quantitative analysis of condyle profiles (n=6). (**I**) Mankin score evaluation (n=6). (**J**) Quantitative

analysis of the proportion of Safranin-O positive areas (n=6). Statistical significance was determined by 1-way ANOVA or Kruskal-Wallis test. Data represent mean ± SD. *$P < 0.05$, **$P < 0.01$, ***$P < 0.001$.